ORIGINAL CONTRIBUTION

Lubricated compression and X-ray microtomography to analyse the rheology of a fibre-reinforced mortar

F. Chalencon · L. Orgéas · P. J. J. Dumont · G. Foray · J.-Y. Cavaillé · E. Maire · S. Rolland du Roscoat

Abstract In this work, the microstructure and the rheology of a glass-fibre-reinforced fresh mortar were studied. Various fibre contents and aspect ratios and two types of fibrous reinforcement, i.e. slender fibre bundles and fibres, were tested. The microstructure was analysed by using X-ray microtomography. It is shown that the non-deformed mortar is a porous granular suspension, the porous microstructure of which is not influenced by the presence of fibres, which in turn display a 2D planar random fibre orientation. The rheology was investigated by subjecting samples to constant axial strain rate and lubricated compression. The roles of the actual strain, the mortar resting time, the fibre content and aspect ratio on recorded stress levels are emphasised. Besides, for the investigated strain rate and material parameters, the mortar flow is quasi-incompressible and does not affect significantly the porous microstructure nor the fibrous one. Lastly, the stress increase which is induced by the addition of fibre bundles is similar to that predicted by Newtonian models of semi-dilute fibre suspensions.

Keywords Fibre suspension · Granular system · Lubricated compression · X-ray microtomography

F. Chalencon · L. Orgéas (✉) · S. Rolland du Roscoat
Laboratoire Sols-Solides-Structures-Risques (3SR),
CNRS/Université de Grenoble (Grenoble INP-UJF),
BP 53, 38041 Grenoble, France
e-mail: Laurent.Orgeas@grenoble-inp.fr

P. J. J. Dumont
Laboratoire de Génie des Procédés Papetiers (LGP2),
CNRS/Institut Polytechnique de Grenoble (Grenoble INP),
BP 65, 38402 Saint-Martin-d'Hères, France

F. Chalencon · G. Foray · J.-Y. Cavaillé · E. Maire
Laboratoire MATEIS, CNRS/INSA de Lyon,
69621 Villeurbanne, France

S. Rolland du Roscoat
European Synchrotron Radiation Facilities, ID19 Beamline,
6, rue Jules Horowitz, 38043 Grenoble, France

Introduction

There is a great interest in adding fibres of various types to cements, concretes or mortars in order to improve their mechanical properties, particularly their ductility and their toughness, as well as their creep properties and their long-term shrinkage behaviour as it is exemplified in some recent experimental studies (Cheng and Liu 2005; Liu et al. 2008; El-Dieb 2009) or theoretical ones (Takashima et al. 2003). The hardened-state properties of these materials have been rather well investigated. On the contrary, there are very few studies, to the best of our knowledge, which focus on the determination of the rheological behaviour of this type of fibre-reinforced materials in their fresh state. Authors who performed the first rheological studies adapted classical "workability" tests such as, for instance, the "slump" test (Grünewald and Walraven 2001; Cheng and Liu 2005; Ferrara et al. 2007; Sahmaran and Yaman 2007). Although a deep analysis of the results given by the slump test can be performed to get quantitative rheological data, as shown in a comprehensive paper by Roussel and Coussot (2005), the slump test, in the above studies, is merely a useful empirical method to class the materials with respect to their ability to be

casted. Only in a study by Ferrara et al. (2007), the way this test was performed revealed experimentally that segregation phenomena might occur for a series of cement pastes. In this study, the tested materials were carefully prepared and reinforced with varying amounts of steel fibres of a given aspect ratio. In Banfill et al. (2006), a rheometer was used to try to get quantitative rheological data for a fibre-reinforced cement mortar. This rheometer made with a cylindrical container and a rotating impeller has the drawbacks of having smaller dimensions compared to the various tested lengths of fibres, although it is well known, for instance in the field of fibrous suspensions, that it is necessary to use large-scale apparatuses to get relevant rheological results. Moreover, this type of rheometer can lead to very particular flow problems such as slip bands, which have to be avoided. In Kuder et al. (2007), a parallel-plate rheometer with an adjustable gap was designed to perform shear tests in order to adjust the dimensions of the rheometer to the length of the tested fibres. This appears as an interesting solution, which has nevertheless the disadvantage to force to a priori assume a given rheological model for exploiting the test results. In the previously cited rheological studies, no tools are presented to assess the microstructure of the tested granular fibrous suspensions before and after subjecting them to mechanical loading. Nevertheless, it is crucial to know the arrangement of the fibres, i.e. their dispersion and orientation, and their evolution to predict the hardened-state properties of such materials as revealed by Ferrara et al. (2008).

In view of the above observations, this study proposes to use lubricated compression tests, which do not require to a priori assume a given rheological model for obtaining quantitative data on the behaviour of a fresh fibre-reinforced mortar. Coupled to this test, some direct observations of the microstructure features (in particular porosity, pore size and fibre orientation) of this mortar before and after testing were performed using the X-ray microtomography. These observations could be carried out using hardened samples but also in some cases using fresh samples by adopting a specific microtomography observation mode. Hence, in "Material", the various constituents together with the processing route used to obtain respectively the fibre-reinforced fresh mortar and the compression samples are presented. The lubricated compression rheometer and the method adopted to extract rheological data from compression tests are given in "Compression rheometry". Compression results ("Rheometry results") and initial and flow-induced microstructures ("Initial and flow-induced microstructures") are shown and finally discussed ("Discussion").

Material

Initial constituents

The used reference mortar is a commercial formulation (Lafarge, Maité monocomposant). The corresponding dry initial pre-mix is composed of more or less spherical grains with various sizes and natures. As shown in Fig. 1, the distribution of the grain diameters, which has been obtained by using a laser granulometer (Malvern Mastersizer 2000), ranges between 2 and 1500 μm and exhibits four grain populations, respectively, between 2 and 10 μm (p_1), 10 and 50 μm (p_2), 50 and 300 μm (p_3) and 300 and 1500 μm (p_4). As revealed by thermal gravimetric analysis and thermal differential analysis measurements (not shown here), the two first populations (p_1, p_2) are essentially composed of cement additives and some polymers ($\approx$6 wt.%), whereas the two other ones (p_3, p_4) are mainly composed of sand, limestone and silica fillers. As soon as water is poured into the granular pre-mix:

− Polymers are dispersed in the liquid phase: they act as lubricants during the deformation of the fresh mortar, and some interactions with cement and filler grains may occur (Knapen and Gemert 2009). Besides, as soon as water is added, micrometric air bubbles can be induced (Atahan et al. 2008).
− Cement hydration begins, i.e. the original cement grains are dissolved, the ionic concentration is increased, and some nanometric hydrates germinate (Thevenin and Pera 1999; Silva and Monteiero 2005). After a few hours, the dispersed polymers together with the newly formed hydrates and the
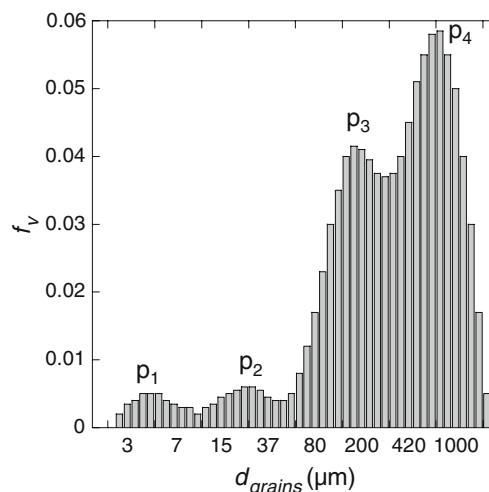

Fig. 1 Particle size distribution within the initial dry pre-mix (obtained from a particle sizer Malvern Master Sizer 2000)

unreacted cement or fillers form a continuous and complex solid network. This network, which is not connected originally within the fresh mortar, will continuously increase its connectivity over months and years.

The reference mortar was reinforced with commercial alkali-resistant glass fibre bundles (Owens Corning, Cemfil Anti-crack). Two types of fibre bundles were used, i.e. high performance (HP) or highly dispersive (HD) ones. They differ in their sizing. In the first case, HP fibre bundles do not disintegrate during both the processing of the mortar and the rheological measurements (*cf.* "Initial and flow-induced microstructures"). On the contrary, as soon as the fresh mortar is prepared, HD bundles disintegrate so that their fibres can be dispersed in the mortar. Five mass fractions of fibre bundles f_m were investigated, i.e. 0 (mortar without fibres), 0.005, 0.01, 0.02 and 0.04. The initial fibre bundles are composed of approximately 200 glass fibres with a diameter $d_f = 14$ μm. They have an elliptical cross section with an equivalent diameter $d_b = \sqrt{d_{max}d_{min}}$, $d_{max} \approx 400 - 800$ μm and $d_{min} \approx 50$ μm being the major and minor axes, respectively (see Table 1). Lastly, four bundle lengths l were used for HP bundles, i.e. 6.1, 10.9, 20.9 and 72 mm, and two for the HD ones, i.e. 5.6 and 11.1 mm (see Table 1). These dimensions were measured ($\approx$50 measurements per fibre type and length) after sample processing (see "Preparation of samples"): (1) by dissolving some fresh samples in water and (2) by proceeding to various filtering operations in order to extract fibres and fibre bundles from the mortar. Hence, when immersed into the fresh mortar, the HP fibre bundles and the dispersed HD fibres can be seen as slender rod-like particles. Their aspect ratios $r = d/l$ ($d \approx d_b$ for bundles and $d = d_f$ for fibres) range from 40 (for the smallest HP bundles) to 793 (for the longest HD fibres). The size d is approximately ten times bigger for the HP ones than for the HD ones, i.e. of the same order as the average size of the bigger grains of the mortar pre-mix (p_3 and p_4, see Fig. 1).

Table 1 Dimensions of the fibres and the fibre bundles (obtained after sample processing)

	HD fibres	HP fibre bundles		
l [mm]	d_f [mm]	d_{min} [mm]	d_{max} [mm]	r
5.6	0.014			400
11.1	0.014			793
6.1		0.05	0.47	40
10.9		0.05	0.7	58
20.9		0.05	0.42	144
72		0.05	0.5	455

Preparation of samples

A special attention was paid to minimise the material variability induced during the preparation of samples. For that purpose, compression samples were processed by following a rigorous protocol:

1. A sufficient amount of pre-mix and water (water/pre-mix weight ratio of 0.17) was mixed by hand for 90 s
2. The prescribed weight fraction of fibres f_m was added, and the whole mixture was mixed for 90 s
3. The as-prepared fresh mortar was thereafter casted into a cylindrical mould
4. The moulded cylindrical samples of axis $\underline{\mathbf{e}}_3$ were then subjected to a lubricated simple precompression along $\underline{\mathbf{e}}_3$ up to a logarithmic axial strain equal to 1 by following the procedure given in "Compression rheometry"
5. The as-pre-deformed samples, which still exhibited nice cylindrical shapes (initial diameters $D_0 = 250$ or 300 mm for the longest HP bundles and $D_0 = 90$ or 150 mm for the other fibrous reinforcement, initial height $h_0 = 14.5$ mm), were finally left at rest for 10 min before the beginning of compression tests. In the following, this time will be arbitrarily named initial time and will be further noted t_0.

By following such a processing route, all samples processed with the same material parameters are expected to display the same initial microstructures with restrained variability. In particular, fibres or fibre bundles should be well distributed within the reference fresh mortar and should lead to a quite pronounced planar random fibre orientation distribution. Besides, it must be pointed out that the dimensions of the initial samples are sufficiently large with respect to the fibres' dimensions and orientation. Hence, provided a good homogeneity of compression experiments (see "Compression rheometry"), a fairly good scale separation is obtained between (1) the macroscopic size of the samples and/or the macroscopic loading and (2) the size of the studied microstructures.

Compression rheometry

The rheology of these fresh samples was studied by using a simple compression rheometer, which was initially developed to study the rheology of highly concentrated fibre suspensions such as short fibre-reinforced polymer composites during their processing (Le Corre et al. 2002; Dumont et al. 2003, 2007; Orgéas et al. 2008).

Compared with standard commercial rheometers, this one allows highly viscous samples with very large dimensions, i.e. larger than the size of the microstructure heterogeneities, to be deformed. Thus, this reduces both scattering of results and possible boundary effects. The rheometer was mounted on a standard mechanical tension–compression testing machine (MTS 4M, load cell 20 kN, maximum crosshead velocity 8 mm s^{-1}).

Tests consisted in compressing lubricated cylindrical samples (initial diameter D_0, initial height h_0) at a constant axial average strain rate $\bar{D}_{33} = \dot{h}/h$ (compression direction given by the unit vector $\underline{\mathbf{e}}_3$) between two horizontal plates parallel to the $(\underline{\mathbf{e}}_1, \underline{\mathbf{e}}_2)$ plane. In this work, a unique axial strain rate $\bar{D}_{33} = 0.1$ s^{-1} was used. Other strain rates will be studied in a further contribution. During each experiment, the sample height h and the axial force F_3 were measured so that the average axial logarithmic strain $\bar{\varepsilon}_{33}$ and stress $\bar{\sigma}_{33}$ could be estimated by $\ln(h/h_0)$ and $4F_3 h_0/(\pi D_0^2 h)$, respectively (assuming the incompressibility of the studied suspensions, *cf.* "Flow kinematics").

Reproducibility and typical compression curves

Figure 2 gives four typical compression stress–strain curves $\bar{\sigma}_{33} - \bar{\varepsilon}_{33}$ obtained with four samples deformed by using the same testing conditions: $D_0 = 150$ mm, $D_{33} = 10^{-1}$ s^{-1}, fresh mortar without fibre, no resting time after t_0.

Firstly, it is worth noting that, due to both the strict processing route and the large samples' dimensions, scattering of the measurements is rather weak and remains below $\pm 10\%$. A similar scattering was recorded when fibres were added to the mortar. Thus, in the following sections, only two compression tests were performed for each testing condition. Results will represent the average of the two tests.

Secondly, it is also worth noting that the shape of stress–strain curves exhibits two distinct stages: stress levels first increase very sharply when $\varepsilon_{33} \leq 0.05$, and then the flow occurs more easily but still with a hardening, which becomes more and more pronounced as the strain increases. This type of results, which emphasises the non-Newtonian behaviour of the mortar, is commonly observed during the compression of concentrated granular and fibre suspensions.

Flow kinematics

In Fig. 2, four photographs are also reported. They correspond to top views of a fifth sample. This latter sample was deformed with the same testing conditions.
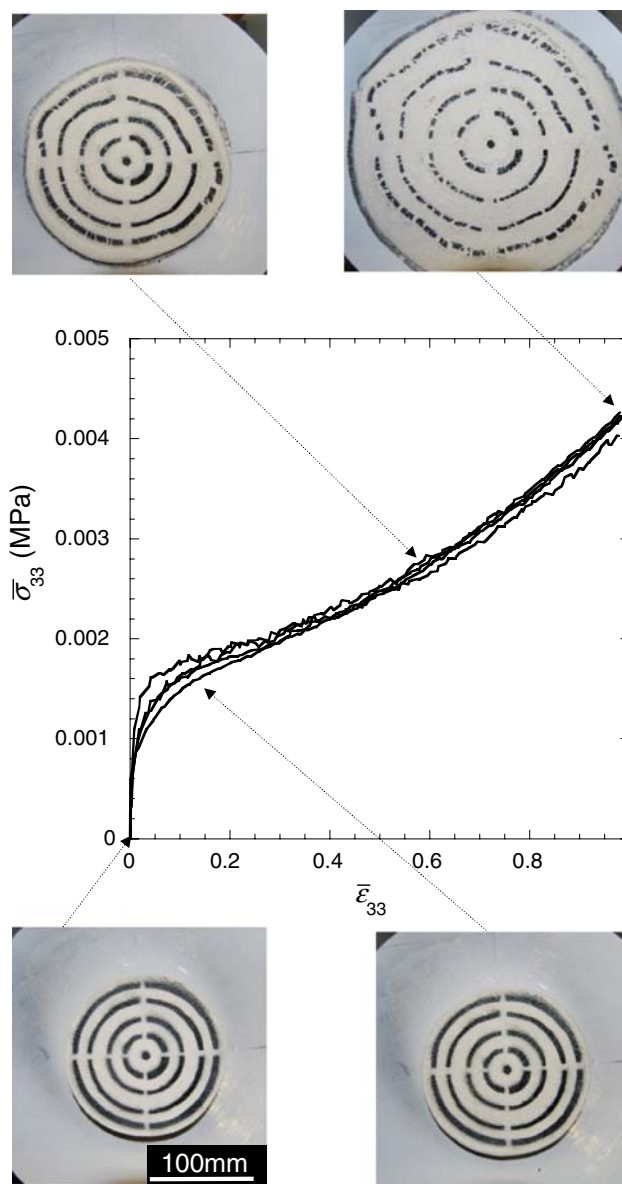

Fig. 2 Typical lubricated compression tests performed at t_0 with the mortar without fibre ($D_0 = 150$ mm). The *graph* represents the stress–strain curves $\bar{\sigma}_{33} - \bar{\varepsilon}_{33}$ for four tests performed using identical testing conditions. *Photographs* show top views of the initial and deformed shapes of a fifth sample at various axial strains

They were taken at various imposed axial strains ε_{33}, i.e. 0, 0.15, 0.6 and 1, as the test was interrupted:

– They showed that marks previously plotted on the sample flowed with no observable sticking zones (Estellé et al. 2006). The lateral vertical surface of the sample, which was initially painted in black, remained likewise quite vertical even at large axial strains. Similar observations were made for fibre-reinforced mortar, at least for the investigated testing conditions.

– The upper surfaces of samples, which were initially circular, remained circular at the macroscale. This was also observed when fibres were added to the mortar, tending to prove that initial and flow-induced microstructures exhibited transverse isotropy (Dumont et al. 2007) (see "Initial and flow-induced microstructures").

– The sample dimensions at the end of the tests were measured and showed that, whatever the fibre content and type, the volume variation, which was induced during flow, was negative but very weak compared to the imposed axial strain, i.e. between −0.02 and 0. It was therefore fair to conclude that the flow of mortar was incompressible.

The above remarks allows us to assume that, due to the lubrication of the compression plates, the Cauchy stress $\underline{\underline{\sigma}}$, the Hencky strain $\underline{\underline{\varepsilon}}$ and the strain rate $\underline{\underline{\mathbf{D}}}$ tensors are homogeneous within flowing samples at the macroscale and read, respectively:

$$\underline{\underline{\sigma}} = \sigma_{33}(\underline{\mathbf{e}}_3 \otimes \underline{\mathbf{e}}_3), \tag{1}$$

$$\underline{\underline{\varepsilon}} = \bar{\varepsilon}_{33}\left(\underline{\mathbf{e}}_3 \otimes \underline{\mathbf{e}}_3 - \frac{1}{2}\underline{\mathbf{e}}_1 \otimes \underline{\mathbf{e}}_1 - \frac{1}{2}\underline{\mathbf{e}}_2 \otimes \underline{\mathbf{e}}_2\right), \tag{2}$$

$$\underline{\underline{\mathbf{D}}} = \bar{D}_{33}\left(\underline{\mathbf{e}}_3 \otimes \underline{\mathbf{e}}_3 - \frac{1}{2}\underline{\mathbf{e}}_1 \otimes \underline{\mathbf{e}}_1 - \frac{1}{2}\underline{\mathbf{e}}_2 \otimes \underline{\mathbf{e}}_2\right). \tag{3}$$

Correction of compression curves

The lubrication layers between the plates and the specimen ensure the flow homogeneity, but they may induce friction forces that may disturb results. For instance, this was clearly observed during lubricated compression of Bulk Mouling Compounds, a glass-fibre-reinforced granular polymer suspension (Orgéas et al. 2008). This is also the case for the present mortar, as revealed in Fig. 3, which shows two homogeneous compression tests performed using fibre-reinforced mortar samples with two different initial diameters D_0, i.e. 90 and 150 mm. Stress levels $\bar{\sigma}_{33}$ are higher for the larger diameter. In order to get rid of such an artefact, for each testing condition: (1) we have systematically performed compression tests with these two initial diameters, (2) we have assumed that the upper and lower surfaces of samples were subjected to tangential stresses $\sigma_{r3} = -\lambda\bar{\sigma}_{33}v_r$ (expressed in the local cylindrical reference frame ($\underline{\mathbf{e}}_r$, $\underline{\mathbf{e}}_\theta$, $\underline{\mathbf{e}}_3$), v_r being the radial velocity), and (3) a reasoning similar to that conducted in Orgéas et al. (2008) was adopted in order to estimate the stress σ_{33} within the samples by:

$$\sigma_{33} = \bar{\sigma}_{33}\left(1 - \frac{\lambda}{16}\frac{\dot{h}}{h^3}h_0 D_0^2\right). \tag{4}$$
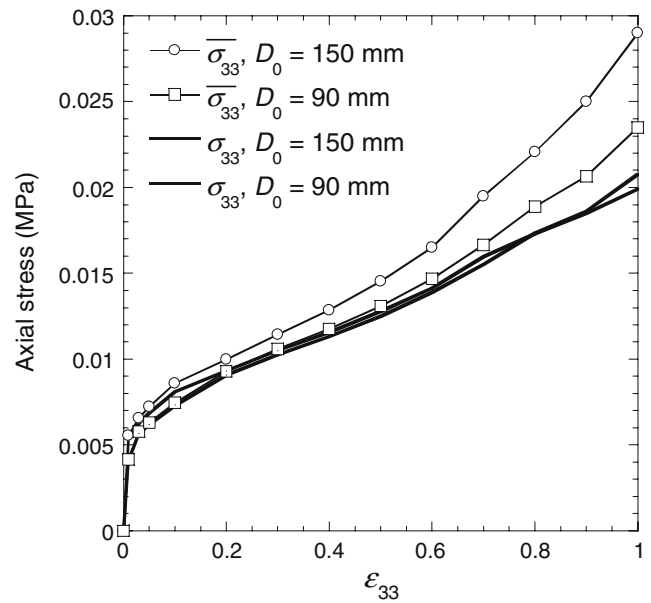

Fig. 3 Influence of the initial sample diameter on stress–strain curves. Correction of the stress–strain curves in order to account for friction between the sample and the rheometer plates. $\bar{\sigma}_{33}$ is the recorded average axial stress, and σ_{33} is the corrected stress that is obtained from Eq. 4. Tests shown were achieved with HD fibre bundles with $l_f = 11$ mm and a resting time $t_r = t_0 + 40$ min. In this case, the corresponding friction coefficient is $\lambda = 1.4\ 10^{-4}$ s mm^{-1}

Hence, by performing two tests with samples of identical formulation but with two different initial diameters D_0, the friction coefficient λ is such that the corrected stress σ_{33} obtained for both tests is superimposed. As revealed by the example given in Fig. 3, by adopting the correction (4), stress–strain curves do not depend on the initial sample diameter any more. Doing so, obtained values of λ were weak and found to range between 2.5×10^{-5} and 0.7×10^{-4} s mm^{-1} for all investigated testing conditions. The recorded variation of the friction coefficient is not very large, although the initial lubrication layer is handmade and therefore may not exhibit a nice reproducibility.

Rheometry results

The influences of the resting time t_r after t_0, the volume fraction of fibres f (estimated from f_m and the specific masses of the fibres and the mortar without fibre) and the aspect ratio r on the rheological behaviour were investigated. Corresponding results are gathered in the graphs of Fig. 4a–f, respectively. This figure brings up the following comments:

– In the stress–strain curves $\sigma^* - \varepsilon_{33}$ of graphs (a, c, e; obtained for some particular mortar formulations),

the dimensionless axial stress σ^* corresponds to the axial stress σ_{33} recorded for the current mortar formulation divided by the axial stress σ_{33} recorded for the so-called reference formulation (further noted σ_{33}^0), i.e. the mortar without fibre at t_0. As shown from these graphs, when the axial strain ε_{33}

is above ≈ 0.05 and whatever both the investigated mortar formulation and the testing conditions, the dimensionless stress σ^* is more or less constant, i.e. it is close to its average value noted $\langle\sigma^*\rangle$ in the graphs of Fig. 4d, f. Hence, for the studied fibrous microstructures and resting times, the strain

Fig. 4 Rheometry results showing the influence of the resting time t_r (**a**, **b**), the fibre volume fraction f (**c**, **d**) and the fibre aspect ratio r (**e**, **f**). Graphs **a**, **c** and **e** give the evolution of the dimensionless axial stress σ^* as a function of the axial strain ε_{33} in the case of the mortar without fibre for various resting times (**a**), no resting time and a fibre aspect ratio $r = 58$ (**c**) and no resting time and a fibre content $f \approx 0.006$ (**e**), respectively. Graphs **b**, **d** and **f** summarise the evolution of ξ^* and $\langle\sigma^*\rangle$ (determined for $0.05 \leq \varepsilon_{33} \leq 1$) as functions of the resting time t_r ($f = 0.006$) (**b**), the fibre content f (HP fibre bundles with $r = 58$ and HD fibres with $r = 793$) (**d**) and the fibre aspect ratio r ($f = 0.006$) (**f**) for all tested conditions. HP fibres bundles are represented by *white marks* whereas HD filaments by *black ones*
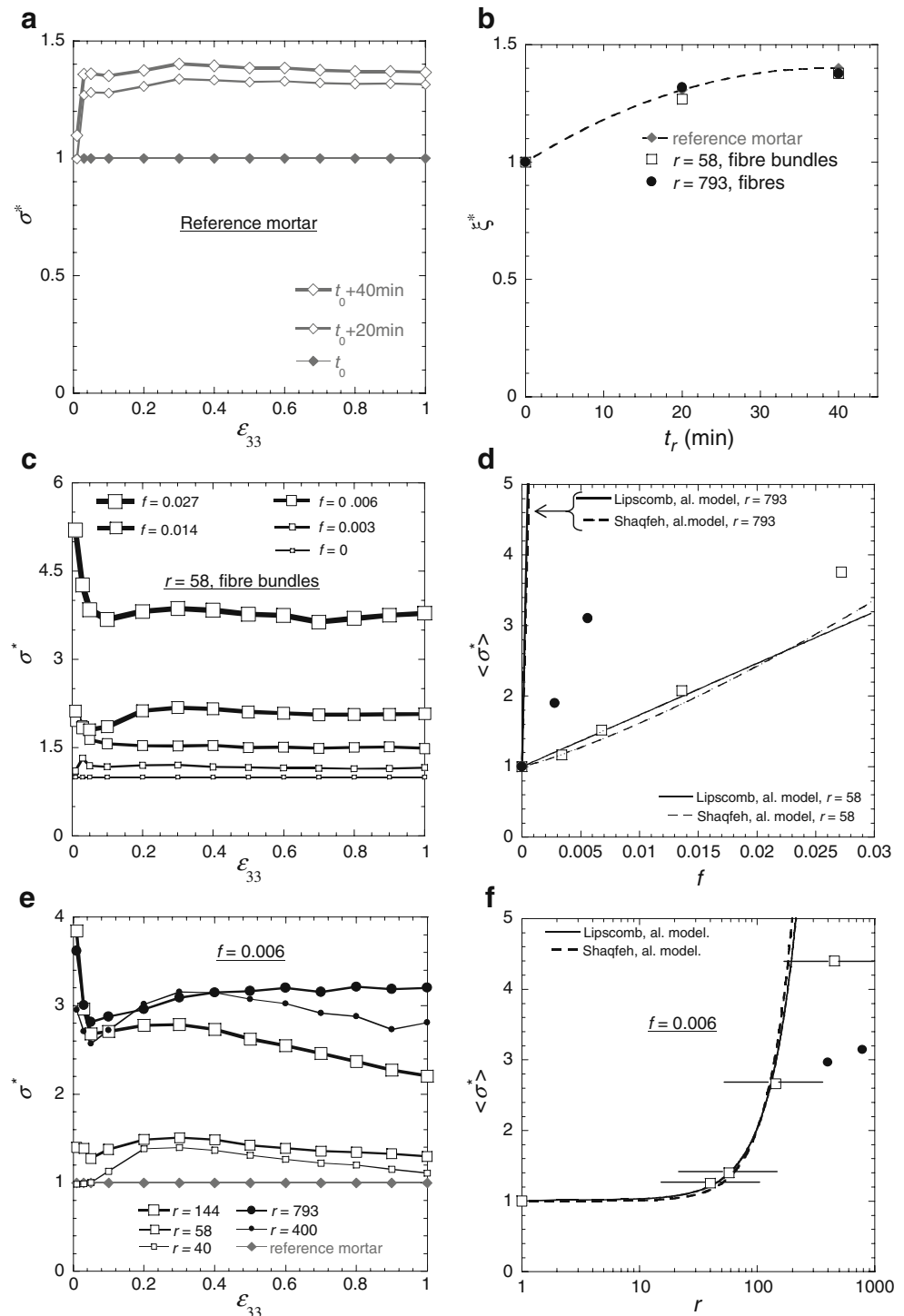
hardening, which is observed for a given formulation, is directly deduced from that recorded for the reference formulation:

$$\sigma_{33} = \sigma_{33}^0(\varepsilon_{33})\sigma^*(t_r, f, r, \text{type of reinforcement}) \quad (5)$$

– The graph (b) gives, for the mortar without or with fibres, the influence of the resting time t_r on the dimensionless ratio $\xi^* = \langle\sigma^*\rangle(t_r)/\langle\sigma^*\rangle(t_0)$, $\langle\sigma^*\rangle(t_r)$ and $\langle\sigma^*\rangle(t_0)$ being obtained for the same mortar formulation but at t_r and t_0, respectively. As evident from this graph, ξ^* increases with t_r. Such an increase is due to the beginning of cement hydration and to possible water evaporation. It must also be pointed out that ξ^* is independent of the fibre content, type and aspect ratio, at least for the investigated fibrous microstructures and resting times. Hence, by noting σ^{0*} the dimensionless stress σ^* obtained for the mortar without fibre at t_r, it is possible to write

$$\sigma^* = \sigma^{0*}(t_r)\sigma^{**}(f, r, \text{type of reinforcement}) \quad (6)$$

where σ^{0*} can for instance be deduced from the graph (b) and where σ^{**} is a dimensionless stress contribution due to the presence of fibres in the mortar (i.e. $\sigma^{**} = 1$ when $f = 0$).

– The role of the volume fraction of fibres f on σ^{**} is emphasised in the graph (d), which gives the evolution of $\langle\sigma^*\rangle$ with f when $t_r = t_0$ (in this case, $\sigma^{**} = \sigma^* \approx \langle\sigma^*\rangle$), for the two types of reinforcement and two aspects ratios. This graph underlines the very strong increase of stress levels with f. For instance, in the case of HP bundles with $r = 58$, $\langle\sigma^*\rangle$ is approximately 3.75 times higher at $f = 0.027$ than that obtained for the mortar without fibre. In the case of very slender HD fibres, such an increase is much more pronounced: for example, at $f \approx 0.006$, the thickening of the mortar is 60% higher for the slender HD fibres than for the shorter HP bundles.

– The roles of the fibre aspect ratio r and the reinforcement type on the rheology of the mortar at t_0 are illustrated in the graph (f) for a fibre content $f \approx 0.006$. As for the fibre content, a noticeable increase of $\langle\sigma^*\rangle$ with r is observed, such an increase being less pronounced for HD filaments. Besides, for approximately the same aspect ratio, i.e. when $r \approx 430$, $\langle\sigma^*\rangle$ is $\approx 50\%$ higher for HP fibre bundles than for HD fibres. Notice that horizontal error bars that have been added in the case of HP bundles correspond to the estimation of the aspect ratio with $d_{\min}$ (lowest values) and with $d_{\max}$ (highest value).

Initial and flow-induced microstructures

Density

Global densities were first obtained in the fresh state at t_0 by simply measuring both the dimensions of the samples and their weight. They were also measured when the samples were solid, i.e. 48 h after t_0. Local densities of each of these samples in the solid state were obtained by simply weighting in air and in water five small cylindrical specimens (diameter = 10 mm), which were extracted along the sample radii. Some of these measurements are summarised in Table 2. As shown from this table:

– The very small fibre content, which was added into the mortar, only slightly increased its density.
– The various measured densities in the various studied states are rather low, indicating that the mortar exhibits porosity. In the case of solid samples, the (open) porosity was estimated by using Hg porosimetry, showing that samples contained approximately a volume fraction of pores (with an open-pore diameter larger than 10 nm) equal to 0.4. In the case of fresh samples, the overall porosity was estimated from the weight fractions and the densities of the fresh mortar constituents, showing for example that the porosity within the fresh mortar without fibre is about 0.24.
– Whatever the fibre content and type, a density loss is observed between t_0 and $t_0 + 48$ h, due to the cement hydration and to water evaporation.
– A very small density variation was recorded along the radius of samples, tending to prove that the sample processing and the compression experiments yielded to negligible microstructure gradients.
– Global and local values of the density were not affected by the compression experiments since they were very close to those of non-deformed samples.

.

Table 2 Global and local densities of some non-deformed and deformed samples

Content, type and length of fibres	ρ at t_0 [g cm^{-3}]	ρ at $t_0 + 48$ h [g cm^{-3}]	ρ_i at $t_0 + 48$ h [g cm^{-3}]
Non-deformed			
0 wt.%,	1.50	1.45	1.45 ± 0.02
1 wt.%, HP, 10.9 mm	1.52	1.45	1.45 ± 0.02
1 wt.%, HD, 11.1 mm	1.54	1.47	1.47 ± 0.02
Deformed			
0 wt.%	1.51	1.45	1.45 ± 0.02
1 wt.% HP 10.9 mm	1.52	1.44	1.44 ± 0.02
1 wt.% HD 11.1 mm	1.54	1.47	1.47 ± 0.02

X-ray microtomography

Other small specimens were also extracted from non-deformed and deformed samples, and their microstructures were analysed by using X-ray microtomography, which allows 2D or 3D representations of the microstructures of heterogeneous materials to be obtained (Baruchel et al. 2006). Such a technique, which is complementary to the MRI (Coussot 2005), was found to give relevant microstructure data during the hydration of cements and plasters (Bentz et al. 2002), as well as before and after the compression moulding of polymer composites reinforced by mineral fillers and fibre bundles (Le et al. 2008). Thus, in order to analyse solid samples (at $t_0 + 24$ h), a laboratory microtomograph (Pheonix Vtomex, INSA Lyon) was used: after the scan of each specimen and the reconstructions of 720 X-ray 2D projections (obtained from the incremental rotation of samples with respect to the X-ray source, scanning time ≈30 min, 90 kV, 140 mA), 3D maps of the X-ray absorption coefficient within each specimen could be obtained (volumes of maximal size of $2000 \times 2000 \times 1500$ voxels, voxel size = 6 μm). Likewise, a fresh cylindrical sample with a diameter of 10 mm and a height of 7 mm was also analysed at t_0 using a synchrotron X-ray microtomograph (ESRF, ID19 Beamline). In this case, the fast X-ray microtomography technique was used (Limodin et al. 2009; Terzi et al. 2009), with a very short scanning time of 1 min (1500 X-ray projections volumes of maximal size of $2000 \times 2000 \times 1000$ voxels, voxel size 7 μm, energy 17 keV, exposure time of 32 ms). Hence, 2D and 3D micrographs of the fresh mortar at t_0 were obtained, with limited microstructural evolutions induced by possible hydration and evaporation.

After suitable filtering operations (achieved with the software Image J), 2D or 3D micrographs such as those given in Fig. 5 in the case of the mortar without fibre at t_0 and $t_0 + 24$ h have been obtained. Notice that the quality of the micrographs given by the fast tomography is lower than that obtained with the standard one: this is due to a lower signal/noise ratio induced by the very short exposure time. Nevertheless, in both cases, resulting micrographs allow fairly nice descriptions of the microstructures : the grey and the white phases represent the various solid phases (p_i, e.g. Fig. 5b), whereas the black one corresponds to pores.

Porosity

We have reported in Fig. 5a the evolution of the grey level (continuous line) along the black horizontal line

displayed in the 2D micrograph of the same figure. This histogram shows that it is possible to extract pores from the other phases of the mortar by simply selecting in greyscale volumes all the voxels below a threshold value of 70. Such a thresholding leads to obtain, for example, the 3D pore microstructure of Fig. 5d (pores have been plotted in white), which corresponds to the 3D micrograph of Fig. 5c.

– This figure shows that the mortar contains a significant amount of pores larger than 6–7 μm. Their corresponding porosity ϕ, simply calculated by the number of white voxels over the total number of voxels, is estimated to be 0.17 ± 0.02 and 0.31 ± 0.02 for the mortar without fibre at t_0 and $t_0 + 24$ h, respectively. This trend, which is obtained only for "big pores", is in good accordance with that obtained in the previous subsection. It is important to notice that whatever the fibre type, content and aspect ratio, this significant porosity was unchanged for the samples that were scanned at $t_0 + 24$ h, as for the density measurements. Please also notice that, whatever the fibre type, content and aspect ratio and for the investigated rheometry conditions, ϕ remains unchanged before and after compression.

– It is also possible to give an estimation of the pore size distribution within the sample with a granulometry algorithm that uses morphological operations together with a hexagonal structural element with a size of eight voxels (Maire et al. 2007). The corresponding results, which have been obtained for analysed volumes of the same size and the same structural element, have been plotted in Fig. 6. Firstly, the graph of Fig. 6a reveals (1) that the major pore size (≈ 200 μm) is not strongly affected by the resting time and (2) that the pore size distribution is wider at $t_0 + 24$ h than that recorded at t_0. Secondly, the graph of Fig. 6a also shows that the pore size distribution $t_0 + 24$ h does not depend on the fibre content and aspect ratio. Lastly, graphs reported in Fig. 6b–d show that the pore size distribution at $t_0 + 24$ h is not significantly affected by the compression without (b) or with fibres (c–d). The slight shift, which is observed, can be related to a rearrangement of the solid particles during compression.

Fibrous microstructures

Figure 7 gives 2D and 3D micrographs of the mortar with fibres. By using another appropriate tuning of the

Fig. 5 **a**, **b** 2D micrographs obtained from X-ray microtomography showing the microstructure of the non-deformed mortar without fibre at t_0 (**a**, fast X-ray microtomography, pixel size = 7 μm, ESRF ID19 Beamline) and at $t_0 + 24$ h (**b**, standard X-ray microtomography, pixel size = 6 μm, MATEIS microtomograph). 3D micrograph of the mortar without fibre at t_0 (**c**) and corresponding porous phase after a suitable thresholding (**d**). The histogram shown in **a** shows (1) the evolution of the grey level (*continuous line*) recorded along the *black line* displayed in the micrograph (**a**) and (2) the threshold value (*dashed-dotted line*) used to obtain the pore microstructure (**d**) from the micrograph (**c**)
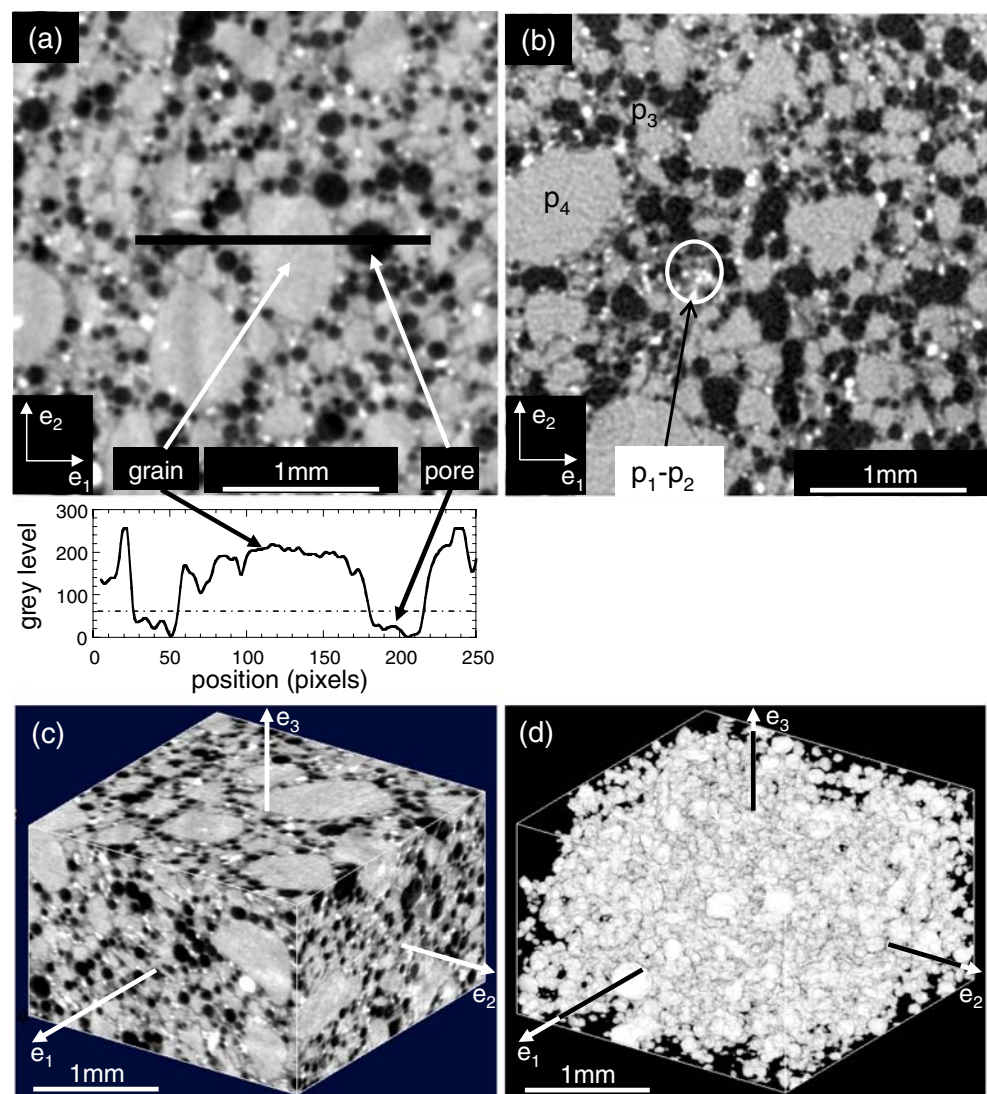

thresholding, i.e. above a greyscale value of 200 (see the greyscale histogram shown in Fig. 7a), it was also possible to separate fibres from the other phases of the mortar. The resulting binarised volumes are illustrated in Fig. 7c, d in the cases of HD fibres (micrograph (c)) and HP fibre bundles (micrograph (d), which is obtained from micrograph (b)):

– As already observed previously, these micrographs confirm that HP fibre bundles have not been disintegrated during the samples' processing (nor after compression), whereas the fibres of the HD ones have been dispersed so that there are no more bundles. However, if HP fibre bundles are rather well dispersed in the material, one can clearly see from Fig. 7c that HD fibres are not homogeneously distributed inside the mortar: some of them form

clusters of aligned fibres, corresponding to the initial bundles they originate from.

– Fibre bundles are straight (see Fig. 7d), whereas some of the fibres, due to their high aspect ratio, have been slightly curved during the processing phase (see Fig. 7c).

– The fibrous reinforcement (fibres or fibre bundles) after processing but also after compression seems to be mainly orientated in the ($\underline{e}_1$, $\underline{e}_2$) plane, with a random orientation in this plane: such a pronounced transverse isotropy has been induced during the pre-compression phase. Due to their quite large size (with respect to the available resolution of the microtomograph), it was possible to determine quantitatively in the case of fibre bundles the fibrous orientation from image analysis by (1) eroding the fibrous phase in order to separate

Fig. 6 Pore size distribution within the non-deformed mortar without and with fibres at t_0 and $t_0 + 24$ h ($f_m = 0.01$, two aspect ratios; **a**), within the non-deformed and deformed mortar without fibre $t_0 + 24$ h (**b**), within the non-deformed and deformed mortar with fibres at $t_0 + 24$ h, i.e. $f_m = 0.01, r = 58$ (**c**), and $f_m = 0.01, r = 793$ (**d**). *Black* and *white marks* correspond to HD fibres and HP fibre bundles, respectively
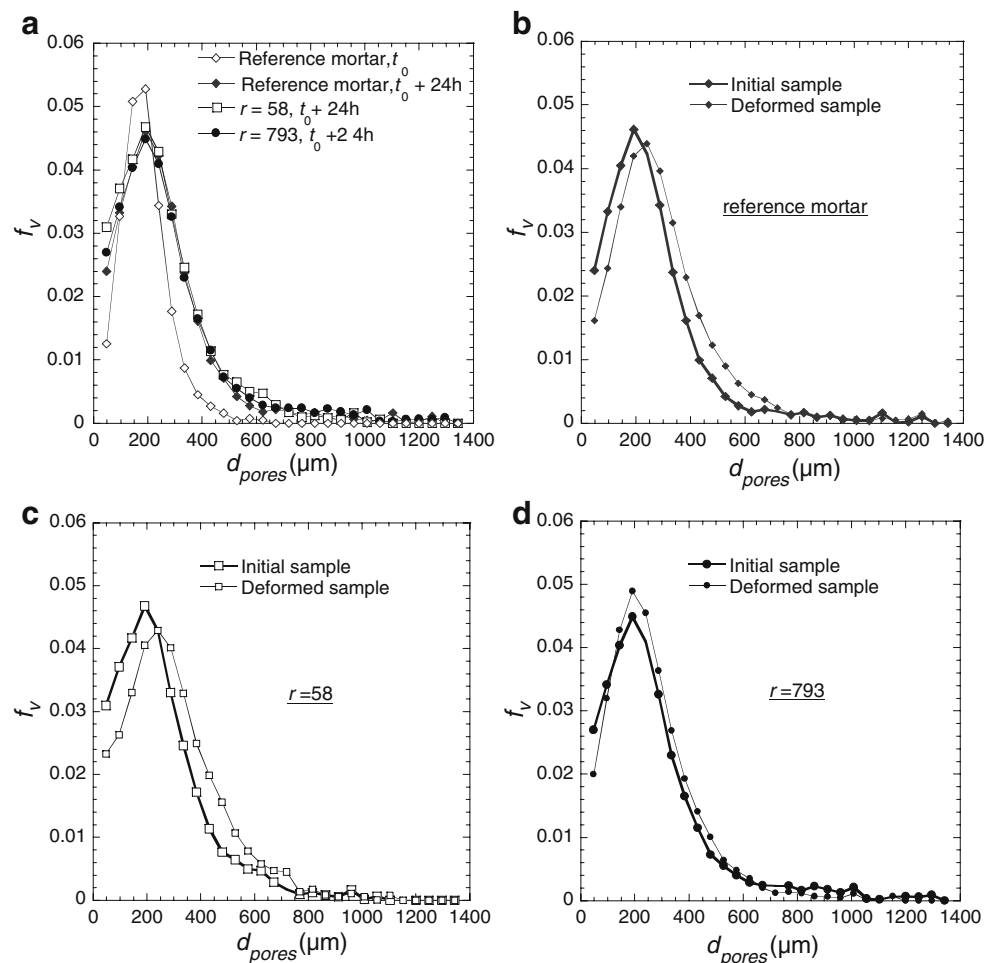
possible contacting bundles, (2) labelling the N isolated bundles, (3) computing their inertia axes, (4) estimating the second-order fibre orientation tensor $\underline{\underline{\mathbf{A}}}$ (Advani and Tucker 1987) by:

$$\underline{\underline{\mathbf{A}}} = \frac{1}{N} \sum_N \underline{\mathbf{p}}_i \otimes \underline{\mathbf{p}}_i, \tag{7}$$

each unit vector $\underline{\mathbf{p}}_i$ corresponding to the principal inertia axis of the labelled bundle i (see Fig. 7d). For instance, the orientation tensors of the non-deformed (*nd*) specimen displayed in Fig. 7a, b, d and of a similar sample after compression respectively read:

$$\underline{\underline{\mathbf{A}}}^{nd} = \begin{bmatrix} 0.58 & 0.02 & 0.01 \\ 0.02 & 0.38 & -0.01 \\ 0.01 & -0.01 & 0.03 \end{bmatrix}_{(\underline{\mathbf{e}}_1, \underline{\mathbf{e}}_2, \underline{\mathbf{e}}_3)} \tag{8}$$

and

$$\underline{\underline{\mathbf{A}}}^{d} = \begin{bmatrix} 0.42 & 0.11 & 0.01 \\ 0.11 & 0.58 & 0.02 \\ 0.01 & 0.02 & 0.00 \end{bmatrix}_{(\underline{\mathbf{e}}_1, \underline{\mathbf{e}}_2, \underline{\mathbf{e}}_3)} \tag{9}$$

Even if such measurement should be carried out for a large number of scanned volumes in order to get more representative results (Dumont et al. 2007), it is nonetheless fair to conclude that (1) the fibrous reinforcements exhibit a planar orientation (the components a_{3i} being very small), with a more or less in-plane isotropy (the components a_{11} being rather close to 0.5).

Discussion

Experimental results gained in the two previous sections lead to the following comments:

1. As shown by X-ray microtomography observations and density measurements (*cf*. Fig. 5 and Table 2), the studied mortar in its fresh or solid states is a porous granular suspension. For the considered imposed strain rate, resting times and fibrous reinforcements, compression experiments showed that the macroscopic flow was homogeneous with no

Fig. 7 Mortar with fibres—2D (**a**) and 3D (**b**) micrographs for the non-deformed mortar with HP fibre bundles ($f_m = 1$ wt.%, $l_f = 10.9$ mm, voxel size $= 25 \mu$m). 3D binarised micrographs showing the fibrous microstructures within non-deformed samples for a fibre content $f_m = 1$ wt.% in cases of (**c**) HD fibres ($l_f = 5.6$ mm, voxel size $= 6 \mu$m) and (**b**) HP fibre bundles ($l_f = 10.9$ mm, voxel size $= 25 \mu$m). The histogram shown in **a** shows (1) the evolution of the grey level (*continuous line*) recorded along the *black line* displayed in the micrograph (**a**) and (2) the threshold value (*dashed-dotted line*) used to obtain the fibrous microstructure (**d**) from the micrograph (**b**)
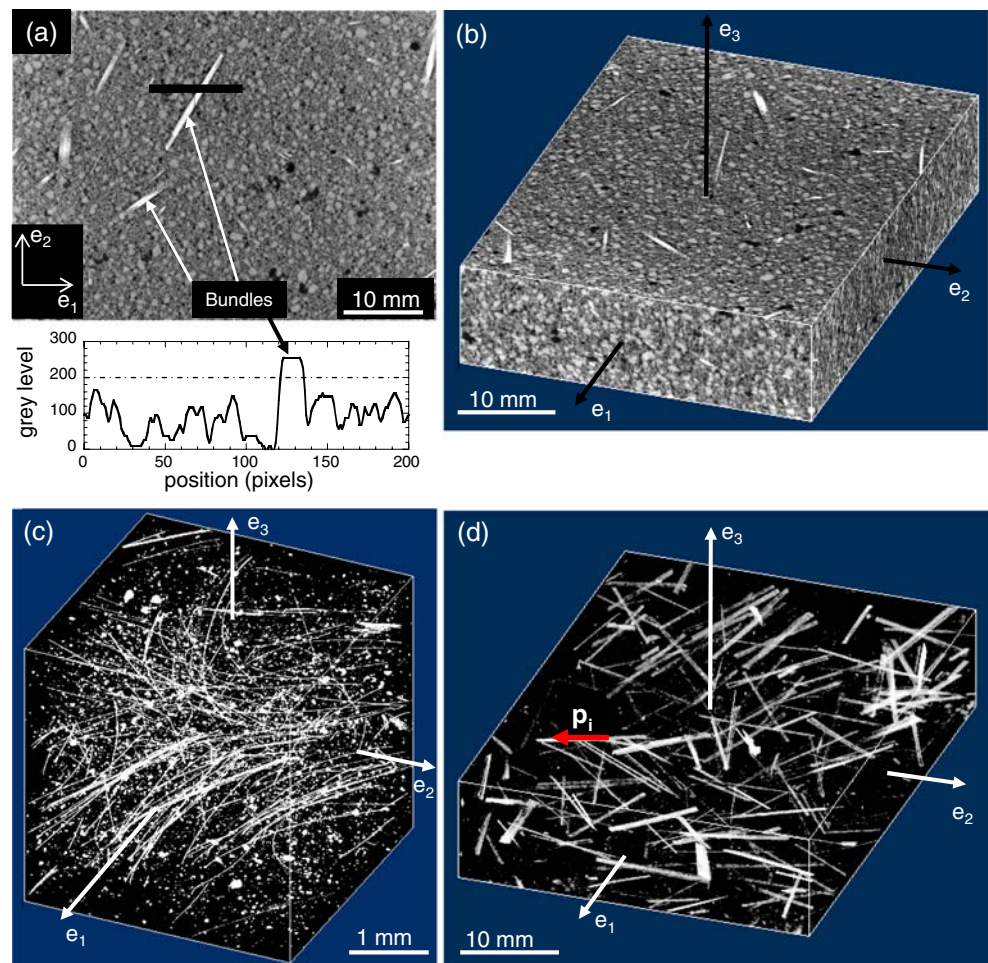
noticeable overall volume variation (with respect to the significant recorded macroscopic deviatoric strain). Besides, local densities and porosities at $t_0 + 24$ h (for pores larger than 48 μm) within samples were found to remain unchanged before and after compression. Consequently, these observations prove that, for the investigated testing conditions, the flow of the studied porous mortar is a homogeneous one-phase and quasi-incompressible flow, without pronounced local consolidation or dilatancy of grains and without liquid phase migration. Other testing conditions, e.g. lower imposed strain rates or other mechanical loadings, should be performed in order to see whether this type of flow still occurs.

2. As revealed in Fig. 4c–f, the fibrous reinforcements thicken the rheology of the mortar. In order to see (*cf.* point 5 below) whether such a thickening is due to mortar–fibre interactions (as in dilute fibre suspensions), to long-range fibre–fibre interactions (as in semi-dilute fibre suspensions) and to possible fibre–fibre short-range interactions (as in concen-

trated fibre suspensions), we have estimated the number of fibre–fibre contacts per fibre C_f within the samples. By assuming that fibres or fibre bundles are straight and well dispersed in the mortar, C_f can be determined from the statistical tube model (Doi and Edwards 1978; Ranganathan and Advani 1991; Toll 1993; Le Corre et al. 2005; Vassal et al. 2008b):

$$C_f = 4f \left(\frac{2}{\pi} r \phi_1 + \phi_2 + 1 \right), \quad (10)$$

where the orientation functions ϕ_i are equal to $2/\pi$ in case of planar fibre orientation (Toll 1993). Hence, according to Eq. 10, C_f is an affine function of f and r. This is illustrated in Fig. 8, which gives the evolution of C_f with f for various values of the aspect ratio r. Marks plotted in the figure correspond to the tested formulations and continuous lines to the prediction given by Eq. 10. Roughly, when C_f is above 2, the fibrous reinforcement forms a continuous network so that the suspension is concentrated. Conversely, when C_f is below 1,
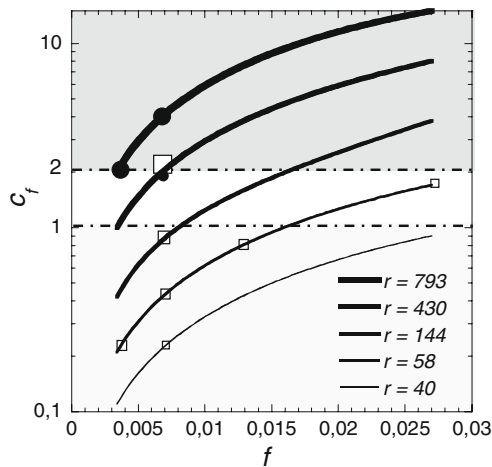
Fig. 8 Evolution (according to the tube model prediction (Eq. 10)) of the number of fibre–fibre contacts per fibre C_f for planar random fibrous networks, as a function of the fibre content f for the various investigated aspect ratios r and types of fibrous reinforcement (*black marks*: HD fibres, *white marks*: HP bundles). *Continuous lines* are the predictions of the tube model. The *darker-grey zone* corresponds to continuous fibrous networks, where the suspension is concentrated. The other *grey zone* corresponds to the semi-dilute regime

the suspension can be considered as semi-dilute. As evident from this figure and according to the estimation given by the tube model, the tested HP formulations can yield to values of C_f below 2 and may be seen as semi-dilute fibre suspensions, whereas the studied HD formulations, due to the high aspect ratio of their fibres, may be considered as concentrated fibre suspensions.

3. The deformed shapes of the initial cylindrical samples are still cylinders. At the same time, fibrous microstructures before and after compression mainly exhibit planar random fibre orientation, i.e. transverse isotropy of axis $\underline{e}_3$, without pronounced evolution. These two macroscopic and microscopic observations are consistent with those already made while compressing highly concentrated planar random fibre bundle polymer suspensions (Dumont et al. 2007). The second one is also consistent with all fibre orientation models based on Jeffery's (1922) equation and its subsequent modifications (Dupret et al. 1999), often used to predict fibre orientation in dilute and semi-dilute Newtonian fibre suspensions. Once again, the fibre-reinforced mortar should be subjected to other mechanical loadings to study more precisely flow-induced fibre orientation.

4. For the studied fibre contents, aspect ratios and types, Eqs. 5 and 6, obtained from rheometry measurements, together with results gained from X-ray

microtomography and density measurements show (a) that the fresh mortar microstructure (and hence its local rheology) is not affected by the presence of fibres or fibre bundles and (b) that its rheology within the fibre suspensions plays a key role on the rheology of the tested fibre-reinforced mortars.

5. In order to better gauge and estimate analytically the coupled roles of the fibre content f and aspect ratio r on the rheology of fibre-reinforced mortars (see Fig. 4d, f), we have estimated the normalised stress σ^{**} given in Eq. 6 in the case of semi-dilute suspensions with incompressible Newtonian suspending fluids, even it is a priori unfair to compare the studied fresh mortar to a Newtonian fluid (see for instance Fig. 2). For that purpose, two well-known rheological models were used. The first one is the model of Lipscomb et al. (1988) (Jeffery 1922; Hand 1961), which is often used to model the rheology of fibre-reinforced polymer composites (Sepehr et al. 2004). The second one is the model developed by Shaqfeh and Fredrickson (1990) (Mackaplow and Shaqfeh 1996) for semi-dilute fibre suspensions. In both cases, the suspension stress tensor $\underline{\underline{\sigma}}$ is split into three contributions:

$$\underline{\underline{\sigma}} = -p\underline{\underline{\delta}} + 2\mu\underline{\underline{D}} + \underline{\underline{\sigma}}^f \tag{11}$$

where the first one involves a pressure p to account for the incompressibility of the suspension; the second one is the contribution of the suspending fluid (shear viscosity μ), and the last one, $\underline{\underline{\sigma}}^f$, is the fibre contribution. For the two considered models, this last term reads, respectively:

$$\underline{\underline{\sigma}}^f = 4\mu f \left(\underline{\underline{D}} + \frac{r^2}{4\ln r}\underline{\underline{\underline{A}}} : \underline{\underline{D}} \right) \tag{12}$$

and

$$\underline{\underline{\sigma}}^f = \frac{4\mu f r^2}{\ln\left(\frac{1}{f}\right) + \ln\left(\ln\left(\frac{1}{f}\right)\right) + C} \left(\underline{\underline{\underline{A}}} - \frac{1}{3}\underline{\underline{\delta}} \otimes \underline{\underline{A}} \right) : \underline{\underline{D}} \tag{13}$$

where C is a constant (the value 0.1585 given by Shaqfeh and Fredrickson (1990) in the case of aligned fibres has been chosen here), and where $\underline{\underline{\underline{A}}}$ is the fourth-order fibre orientation tensor (Advani and Tucker 1987). Its components A_{ijkl} were estimated from those of $\underline{\underline{A}}$ in the case of 2D planar

random fibre orientation, by using the natural closure approximation (Dupret et al. 1999):

$$A_{ijkl} = \frac{1}{3}(A_{ij}A_{kl} + A_{ik}A_{lj} + A_{il}A_{jk})$$

$$+ \frac{1}{6}(\delta_{ij}\delta_{kl} + \delta_{ik}\delta_{lj} + \delta_{il}\delta_{jk})\det\underline{\underline{\mathbf{A}}}, \qquad (14)$$

which is exact in the case of planar random fibrous networks (Dupret et al. 1999). Thus, by combining the above constitutive equations when considering the lubricated compression of incompressible Newtonian fibre suspensions exhibiting 2D planar fibre orientation (in the ($\underline{\mathbf{e}}_1$, $\underline{\mathbf{e}}_2$) plane), it is possible to get estimates of σ^{**}, i.e.:

$$\sigma^{**} = 1 + f\left(2 + \frac{r^2}{12\ln r}\right) \qquad (15)$$

for the model of Lipscomb et al. and

$$\sigma^{**} = 1 + \frac{fr^2}{9\left(\ln\left(\frac{1}{f}\right) + \ln\left(\ln\left(\frac{1}{f}\right)\right) + C\right)} \qquad (16)$$

for the model of Shaqfeh and Fredrickson. These two expressions emphasise the coupled role of f and r. For comparison, they have been reported in the two graphs (d) and (f) of Fig. 4:

– For the HP fibre bundles, both estimates are astonishingly close to the experimental data and give the correct trend, despite the very strong differences of rheology between the model incompressible Newtonian fluid and the studied porous and granular fresh mortar. Such a result should therefore be carefully considered, at least from a quantitative point of view. Other experiments, performed at various strain rates to gauge the non-Newtonian rheology of the mortar, should be required to confirm these results.

– For the very slender HD filaments, both Newtonian semi-dilute predictions are much higher than the current experimental data. As the studied HD mortar formulations can fall into the concentrated regime (see Fig. 8), a first proposition to explain such a discrepancy would consist in considering possible efforts induced by fibre–fibre contacts: this would lead to add another stress contribution to $\underline{\underline{\sigma}}^f$ (Toll and Månson 1994; Servais et al. 1999; Le Corre et al. 2004, 2005; Djalili-Moghaddam and Toll 2005; Férec et al. 2009; Dumont et al. 2009). Nonetheless, this would yield an additional

increase of trends proposed by semi-dilute models and hence would further increase the difference between predictions of models and experimental results. Another possible explanation comes from the HD fibrous microstructures. As revealed from X-ray microtomography (see Fig. 7b), some of the HD filaments are curved, even before compression: such a curvature can therefore yield a decrease of the number of fibre–fibre contacts C_f lower than the value predicted by the very simple tube model (Eq. 10). This can also induce a possible decrease of the effective aspect ratio r used for semi-dilute models of straight fibres and so a decrease of σ^{**}. Similarly, and more probably, it has been emphasised from Fig. 7b that HD filaments form some clusters of fibres. In a sense, these clusters can be viewed as big slender objects the aspect ratio of which is much lower than that of the HD filaments: thus, this can yield a significant decrease of the overall fibre aspect ratio of the suspension and so a decrease of σ^{**}.

Conclusions

In this work, the rheology of a fibre-reinforced fresh mortar was analysed by using both lubricated compression at a moderate strain rate and X-ray microtomography. Conclusions drawn from the present study can be summarised by the following points:

– Provided both a careful processing of samples and the use of a rheometer, the dimensions of which are larger than those of the material heterogeneities, reproducible rheometry experiments can be gained, allowing quantitative trends to be obtained.

– The density measurements combined with X-ray microtomography show that the tested fresh mortar is a porous granular suspension. Its rheology exhibits a hardening that depends on the imposed axial strain and the resting time before compression. Its porous microstructure is not drastically modified by the addition of a weak amount of fibres, nor by the compression flow. Besides, no noticeable consolidation or dilatancy of grains and no liquid phase migration are observed, at least for the investigated testing conditions. This point will be further explored.

– Produced fibre-reinforced mortar samples display a 2D planar random fibre orientation, which does not appear to be affected by the compression flow.

– The addition of fibres in the mortar significantly increases stress levels to induce the suspension flow. However, stress–strain curves can be scaled by the one obtained for the mortar without fibre. Such an increase is a function of the fibre type (HP fibre bundles or HD filaments), content and aspect ratio. In the case of HP fibre bundles, it is similar to that proposed for incompressible semi-dilute Newtonian suspensions containing well-dispersed and straight fibres. This result does not hold for the studied HD filaments: the remaining fibre clusters, which have not been fully dispersed during the processing phase, are presumably responsible for this trend.

References

Advani SG, Tucker CL (1987) The use of tensors to describe and predict fiber orientation in short fiber composites. J Rheol 3(8):751–784

Atahan H, Carlos J et al (2008) The morphology of entrained air voids in hardened cement paste generated with different anionic surfactants. Cem Concr Compos 30:566–575

Banfill P, Starrs G, Derruau G, McCarter W, Chrisp T (2006) Rheology of low carbon fibre content reinforced cement mortar. Cem Concr Compos 28:773–780

Baruchel J, Buffiere J, Cloetens P, Di Michiel M, Ferrie E, Ludwig W, Maire E, Salvo L (2006) Advances in synchrotron radiation microtomography. Scr Mater 55:41–46

Bentz D, Mizell S, Satterfield S, Devaney J, George W, Ketcham P, Graham J, Quenard D, Vallee F, Sallee H, Boller E, Baruchel J (2002) The visible cement data set. J Res Natl Inst Stand Technol 107:137–148

Cheng B, Liu J (2005) Contribution of hybrid fibers on the properties of the high-strength lightweight concrete having good workability. Cem Concr Res 35:913–917

Coussot P (2005) Rheometry of pastes, suspensions and granular materials: applications in industry and environment. Wiley, New York

Djalili-Moghaddam M, Toll S (2005) A model for short-range interactions in fibre suspensions. J Non-Newton Fluid Mech 132:73–83

Doi M, Edwards SF (1978) Dynamics of rod-like macromolecules in concentrated solution. J. Chem Soc Faraday Trans II 74(1):560–570

Dumont P, Orgéas L, Le Corre S, Favier D (2003) Anisotropic viscous behaviour of sheet molding compounds (SMC) during compression molding. Int J Plast 19(4):625–646

Dumont P, Vassal J-P, Orgéas L, Michaud V, Favier D, Månson J-E (2007) Processing, characterization and rheol-

ogy of transparent concentrated fibre bundle suspensions. Rheol Acta 46:639–651

Dumont PJJ, Le Corre S, Orgéas L, Favier D (2009) A numerical analysis of the evolution of bundle orientation in concentrated fibre-bundle suspensions. J Non-Newton Fluid Mech 160:76–92

Dupret F, Couniot A, Mal O, Vanderschuren L, Verhoyen O (1999) Modelling and simulation of injection molding. Rheology series. Elsevier, Amsterdam, pp 939–1010

El-Dieb AS (2009) Mechanical, durability and microstructural characteristics of ultra-high-strength self-compacting concrete incorporating steel fibers. J Mater Design 30:4286–4292

Estellé P, Lanos C, Perrot A, Servais C (2006) Slipping zone location in squeeze flow. Rheol Acta 45:444–448

Férec J, Ausias G, Heuzey MC, Carreau PJ (2009) Modeling fiber interactions in semiconcentrated fiber suspension. J Rheol 53:49–72

Ferrara L, Park Y-D, Shah SP (2007) A method for mix-design of fiber-reinforced self-compacting concrete. Cem Concr Res 37:957–971

Ferrara L, Park Y-D, Shah SP (2008) Correlation among fresh state behavior, fiber dispersion, and toughness properties of sfrcs. J Mater Civ Eng 20(7):493–501

Grünewald S, Walraven JC (2001) Parameter study on the influence of steel fibers and coarse aggregate content on the fresh properties of self-compacting concrete. Cem Concr Res 31:1793–1798

Hand GL (1961) A theory of dilute suspensions. Arch Ration Mech Anal 7:81–86

Jeffery GB (1922) The motion of ellipsoidal particles immersed in a viscous fluid. Proc R Soc London A 102:161–179

Knapen E, Gemert DV (2009) Cement hydration and microstructure formation in the presence of water soluble polymers. Cem Concr Res 39:6–13

Kuder KG, Ozyurt N, Mu EB, Shah SP (2007) Rheology of fiber-reinforced cementitious materials. Cem Concr Res 37:191–199

Le TH, Dumont PJJ, Orgéas L, Favier D, Salvo L, Boller E (2008) X-ray phase contrast microtomography for the analysis of the fibrous microstructure of SMC composites. Compos Part A 39:91–103

Le Corre S, Orgéas L, Favier D, Tourabi A, Maazouz A, Venet C (2002) Shear and compression behaviour of sheet molding compounds. Compos Sci Technol 62(4):571–577

Le Corre S, Caillerie D, Orgéas L, Favier D (2004) Behavior of a net of fibers linked by viscous interactions: theory and mechanical properties. J Mech Phys Solids 52:395–421

Le Corre S, Dumont P, Orgéas L, Favier D (2005) Rheology of highly concentrated planar fiber suspensions. J Rheol 49:1029–1058

Limodin N, Salvo L, Boller E, Suéry M, Felberbaum M, Gailliègue S, Madi K (2009) In situ and real-time 3-D microtomography investigation of dendritic solidification in an Al 10 wt.% Cu alloy. Acta Mater 57:2300–2310

Lipscomb GG, Denn MM, Hur DU, Boger DV (1988) The flow of fiber suspensions in complex geometries. J Non-Newton Fluid Mech 26:297–325

Liu X-J, Yu Z-W, Jiang L-Z (2008) Long term behavior of self-compacting reinforced concrete beams. J Cent South Univ Technol 15:423–428

Mackaplow MB, Shaqfeh ESG (1996) A numerical study of the rheological properties of suspensions of rigid, non-brownian fibres. J. Fluid Mech 329:155–186

Maire E, Colombo P, Adrien J, Babout L, Biasetto L (2007) Characterization of he morphology of cellular ceramics by

3D image processing of X-ray tomography. J Eur Ceram Soc 27:1973–1981

Orgéas L, Dumont PJJ, Le TH, Favier D (2008) Lubricated compression of BMC, a concentrated and fibre reinforced granular polymer suspension. Rheol Acta 47:677–688

Ranganathan S, Advani SG (1991) Fiber–fiber interactions in homogeneous flows of non-dilute suspensions. J Rheol 35:1499–1522

Roussel N, Coussot P (2005) "Fifty-cent rheometer" for yield stress measurements: from slump to spreading flow. J Rheol 49(3):705–718

Sahmaran M, Yaman IO (2007) Hybrid fiber reinforced self-compacting concrete with a high-volume coarse fly ash. Constr Build Mater 21:150–156

Sepehr M, Ausias G, Carreau PJ (2004) Rheological properties of short fiber filled polypropylene in transient shear flow. J Non-Newton Fluid Mech 123:19–32

Servais C, Månson J-AE, Toll S (1999a) Fiber-fiber interaction in concentrated suspensions: disperse fibers. J Rheol 43(4):991–1004

Shaqfeh ESG, Fredrickson G (1990) The hydrodynamic stress in a suspension of rods. Phys Fluids 2(1):7–24

Silva D, Monteiero P (2005) Hydration evolution of c3s-eva composites analysed by soft X ray microscopy. Cem Concr Res 35(2):351–357

Takashima H, Miyagai K, Hashida T, Li VC (2003) Ia design approach for the mechanical properties of polypropylene discontinuous fiber reinforced cementitious composites by extrusion molding. Eng Fract Mech 70:853–870

Terzi S, Salvo L, Suéry M, Boller E (2009 In situ X-ray micro-tomography characterization of the entrapped liquid formed during partial remelting of a cold-rolled Al8 wt.% Cu alloy. Scr Mater 60(8):671–674

Thevenin G, Pera J (1999) Interactions between lead and different binders. Cem Concr Res 29:1605–1610

Toll S (1993) Note: on the tube model for fiber suspensions. J Rheol 37(1):123–125

Toll S, Månson J-AE (1994) Dynamics of a planar concentrated suspension with non-hydrodynamic interaction. J Rheol 38(4):985–997

Vassal J-P, Orgéas L, Favier D, Auriault J-L, Corre SL (2008b) Upscaling the diffusion equations in particulate media made of highly conductive particles. II. Application to fibrous materials. Phys Rev E 77:011303